JOURNAL OF MATERIALS SCIENCE 32 (1997) 1877–1887

Investigation of the effects of microstructure on creep deformation in α_2-based titanium aluminide intermetallics

W. O. SOBOYEJO
Department of Materials Science and Engineering, The Ohio State University, 116 West, 19th Avenue, Columbus, OH 43210, USA

R. J. LEDERICH, D. S. SCHWARTZ
McDonnell Douglas Corporation, P. O. Box 516, St. Louis, MO 63166, USA

The results of a systematic investigation of the effects of microstructure/substructure on the secondary creep behaviour of α_2-based titanium aluminide alloys are presented. This includes a study of the effects of heat treatment on the steady-state creep behaviour of $\alpha_2 + \beta$-processed Ti–24Al–11Nb and Ti–25Al–10Nb–3V–1Mo at 540, 650 and 760 °C, and an investigation of the effects of creep deformation on dislocation substructures in Ti–24Al–11Nb. The parameters that control secondary creep deformation are identified for both alloys, and the results are compared with data obtained for conventional high-temperature near-α titanium alloys and β-forged Ti–24Al–10Nb–3V–1Mo.

1. Introduction

There have been intensive efforts in recent years to develop α_2-based titanium aluminide alloys with a good balance of elevated-temperature creep and oxidation resistance, and room-temperature fracture properties [1–3]. However, although the tensile deformation [4, 5] and fracture behaviour [4–9] have received attention, there have been few systematic investigations of the creep behaviour [10, 11] of these alloys. Previous studies include an investigation of steady-state creep in Ti_3Al + 10 wt % Nb by Mendiratta and Lipsitt [10] and a recent study of the effects of microstructure on the creep behaviour of β-forged super-α_2 (Ti–24Al–10Nb–1V) [11]. Both studies reported steady-state creep exponents that indicated transitions in the micromechanisms of creep deformation at high stresses and temperatures. However, the micromechanisms of primary and secondary creep deformation and the effects of microstructure/substructure were not examined in detail for the wide range of microstructures that can be produced in this class of alloys.

The results of a systematic study of the effects of microstructure and substructure on the secondary creep behaviour of $\alpha_2 + \beta$-forged Ti–24Al–11Nb and $\alpha_2 + \beta$-rolled Ti–25Al–10Nb–3V-1Mo are reported in this paper. The effect of continuous, contiguous, and Widmanstatten $\alpha_2 + \beta$ microstructures on steady-state creep behaviour are reported, and a discussion of the effect of creep deformation on the substructure of Ti–24Al–11Nb is presented. The parameters that control secondary creep deformation in Ti–24Al–11Nb and Ti–25Al–10Nb–3V-1Mo are identified from the creep exponents, and the steady-state creep data obtained are compared to data obtained for conventional high-temperature near-α titanium alloys [12, 13] and β-forged Ti–25Al–10Nb–3V–1Mo [11].

2. Experimental procedure

The powder metallurgy Ti–24Al–11Nb alloy was supplied by the Alcoa Research Center, PA. It was produced by drop forging into a pancake shape with a thickness of 12.3 mm and a diameter of $\sim$ 260 mm. Forging was carried out in multiple steps at temperatures close to the β solvus (1035 °C). The forged billet was subsequently annealed at 1093 °C for 0.5 h and fan-air-cooled (FAC) to produce a Widmanstatten microstructure with aligned colonies of $\sim$ 3 μm wide α_2 platelets in a matrix of β phase (Fig. 1a).

The ingot metallurgy Ti–25Al–10Nb–3V–1Mo alloy was supplied by TIMET, Henderson, NV. It was produced by rolling of ingots to 10 mm thick plate and β annealing at 1200 °C prior to pack rolling to sheet form in the $\alpha_2 + \beta$ phase field. Pack rolling was performed close to the β solvus (1053 °C) at 1000 °C. Rolling was conducted at a strain rate of $2\,s^{-1}$ and reduction ratios of 10%–15% per pass. The final sheet thickness was $\sim$ 1.25 mm. The resulting sheet product was then mill-annealed at 982 °C for 0.5 h prior to air-cooling. This resulted in the partially recrystallized duplex $\alpha_2 + \beta$ microstructure shown in Fig. 1b. The actual compositions of the as-received alloys are shown in Table I.

The creep testing of Ti–24Al–11Nb was conducted on 6.35 mm × 6.35 mm × 6.35 mm cubic specimens

0022–2461

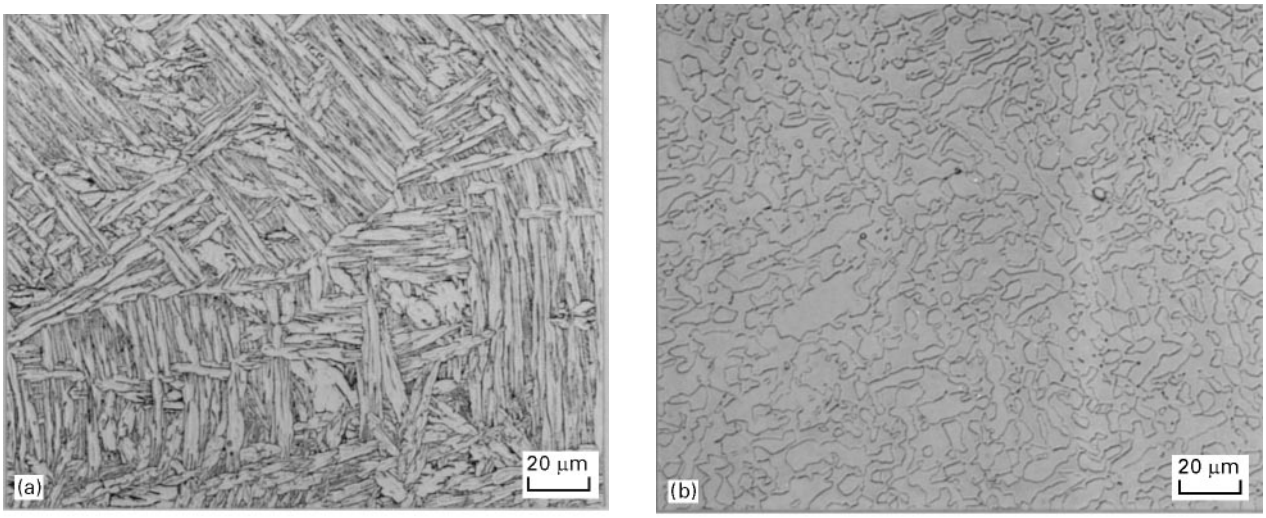

Figure 1 Microstructures of as-received alloys (a) Ti–24Al–11Nb (1093 °C/0.5 h/FAC) and (b) Ti–25Al–10Nb–3V–1Mo (982 °C/0.5 h/AC).

TABLE I Actual compositions (wt %) of as-received alloys Ti–24Al–11Nb and Ti–25Al–10Nb–3V–1Mo

Alloy	Tl	Al	Nb	O	N	C	H	Fe	V	Mo
Ti–24Al–11Nb	Balance	13.4	22.1	0.075	0.0078	0.017	0.0042			
Ti–25Al–10Nb–3V–1Mo	Balance	14.4	19.4	0.09	0.006	0.021	0.006	0.08	3.3	2.0

under compression loading conditions. The tests were performed in air at 540, 650, and 760 °C, and the initial stress ranges were between 70 and 420 MPa. Secondary creep rates were determined at a minimum of four stress levels per temperature, and a load-increasing schedule was employed during the tests, i.e. loads were increased after extensive secondary creep deformation at lower load levels, thus making it possible to obtain multiple secondary creep-rate data (for a particular temperature) over a wide stress range from a single cubic specimen.

The steady-state creep tests on the Ti–25Al–10Nb–3V–1Mo sheet were performed in tension using specimens with rectangular (6.35 mm × 0.635 mm) cross-sections. The tests were conducted in air at 540, 650, and 760 °C using initial stress ranges between 70 and 900 MPa. A load-increasing schedule similar to that described above for Ti–24Al–11Nb was employed in the testing of the Ti–25Al–10Nb–3V–1Mo sheet.

Because the objective of the study was to investigate the effect of microstructure on the creep behaviour of α_2-based alloys, a preliminary investigation of the effects of annealing on the microstructural evolution of the Ti–24Al–11Nb forging and the Ti–25Al–10Nb–3V–1Mo sheet was conducted. This revealed that the two basic types of microstructure that could be achieved by simple heat treatment of the Ti–24Al–11Nb alloy are: (a) a colony Widmanstatten microstructure with $\sim 3\,\mu m$ wide α_2 laths in a β matrix produced by annealing solely in the $\alpha_2 + \beta$ phase field at 815 °C/5.5 h/AC or 982 °C/4 h/AC (Fig. 2a, b), and (b) a transformed Widmanstatten microstructure with large ($\sim 1000\,\mu m$) prior β grains and $\sim 3\,\mu m$ wide elongated α_2 grains within the prior β grains which was produced by annealing at 1200 °C/0.5 h/AC + 760 °C/8 h/AC (AC = air cool) or 1200 °C/0.5 h/AC + 815 °C/8 h/AC (Fig. 2c–f).

Three unique types of microstructure were identified after heat treatment of the Ti–25Al–10Nb–3V–1Mo alloy. A microstructure with contiguous α_2 and grains was obtained by annealing in the $\alpha_2 + \beta$ phase field at 760 °C/24 h/AC (Fig. 3a); a continuous $\alpha_2 + \beta$ microstructure obtained by annealing at 1045 °C/0.5 h/AC as shown in Fig. 3b. Note that this microstructure transformed back to a contiguous $\alpha_2 + \beta$ microstructure after furnace cooling (FC) from 1045 °C to room-temperature and annealing at 760 °C/24 h/AC, as shown in Fig. 3c. Nevertheless, the microstructure produced by annealing at 1045 °C/0.5 h/FC + 760 °C/24 h/AC (Fig. 3c) will be referred to as the "continuous" microstructure to distinguish it from the other microstructures. Finally, a transformed Widmanstatten microstructure with very fine acicular α_2 grains within large prior β grains was produced by annealing at 1200 °C/0.5 h/AC + 760 °C/45 h/AC (Fig. 3d). Note that grain-boundary α_2 was observed along the prior β grain boundaries of both the Ti–24Al–11Nb and Ti–25Al–10Nb–3V-1Mo alloys after annealing in the β and $\alpha_2 + \beta$ phase fields (Figs 2c–e and 3d).

The microstructures that were employed in the creep tests were found to be stable during creep deformation at 760 °C for 20 h, as shown in Figs 4 and 5. The trends in the creep data reported in this paper cannot, therefore, be attributed to microstructural instabilities during creep deformation at elevated temperatures. It is also important to note that the increase in the interstitial oxygen content during testing was always less than 0.025 wt %. After testing, transverse cross-sections, i.e. cross-sections taken in the long

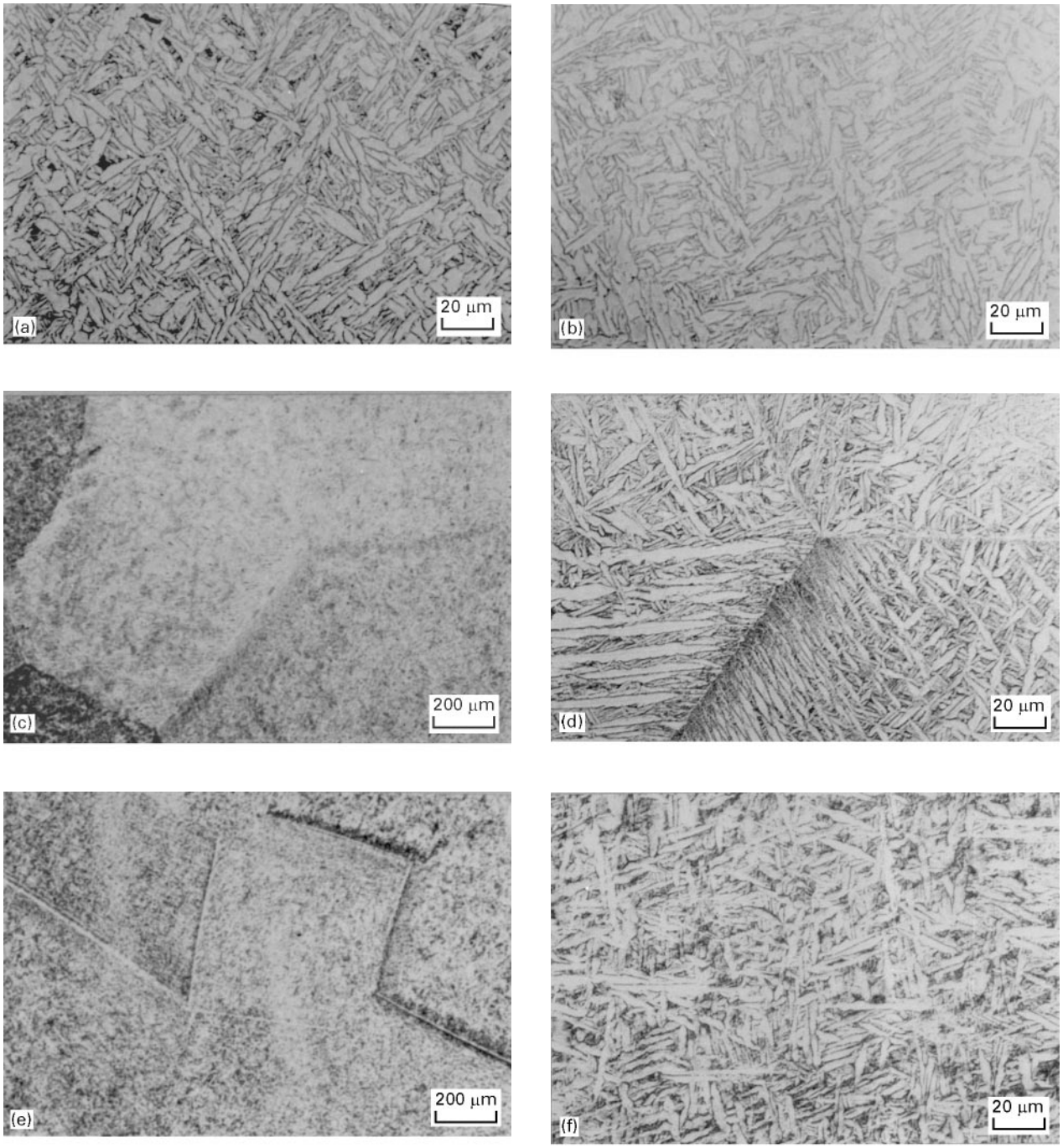

Figure 2 Effects of heat treatment on the microstructure of Ti–24Al–11Nb (a) 815 °C/5.5 h/AC, (b) 982 °C/4 h/AC, (c, d) 1200 °C/0.5 h/AC + 760 °C/8 h/AC, and (e, f) 1200 °C/0.5 h/AC − 815 °C/8 h/AC.

transverse plane, of the Ti–24Al–11Nb creep specimens, were examined by transmission electron microscopy to study the microstructure and the dislocation networks that were introduced during creep deformation. Wafers were cut from the deformed specimens with a diamond saw. These were mechanically ground to a thickness of ~ 100 μm before punching out circular discs (~ 3 mm diameter) which were electrolytically polished in a 5% solution of perchloric acid in methanol prior to TEM examination.

3. Results and discussion

3.1. Ti–24Al–11Nb

The secondary creep-rate data obtained for Ti–24Al–11Nb are summarized in Fig. 6. These data show that heat treatment has very little effect on the secondary creep behaviour at 650 and 760 °C. However, a significant effect of heat treatment was observed at 540 °C, where the lowest secondary creep rates were observed after annealing at 1200 °C/0.5 h/AC + 815 °C/8 h/AC. This heat treatment, like most of the others, resulted in anomalous two-stage (dual slope) secondary creep behaviour during testing at 650 and 760 °C. Reasons for this anomalous behaviour are not understood at present. However, Thompson [14] observed similar two-stage secondary creep behaviour which he attributed to inconsistencies in the creep-testing conditions because the dual-slope steady-state creep curves could not always be reproduced in duplicate tests. However, it is also possible that the change in slope of the secondary creep curve might be

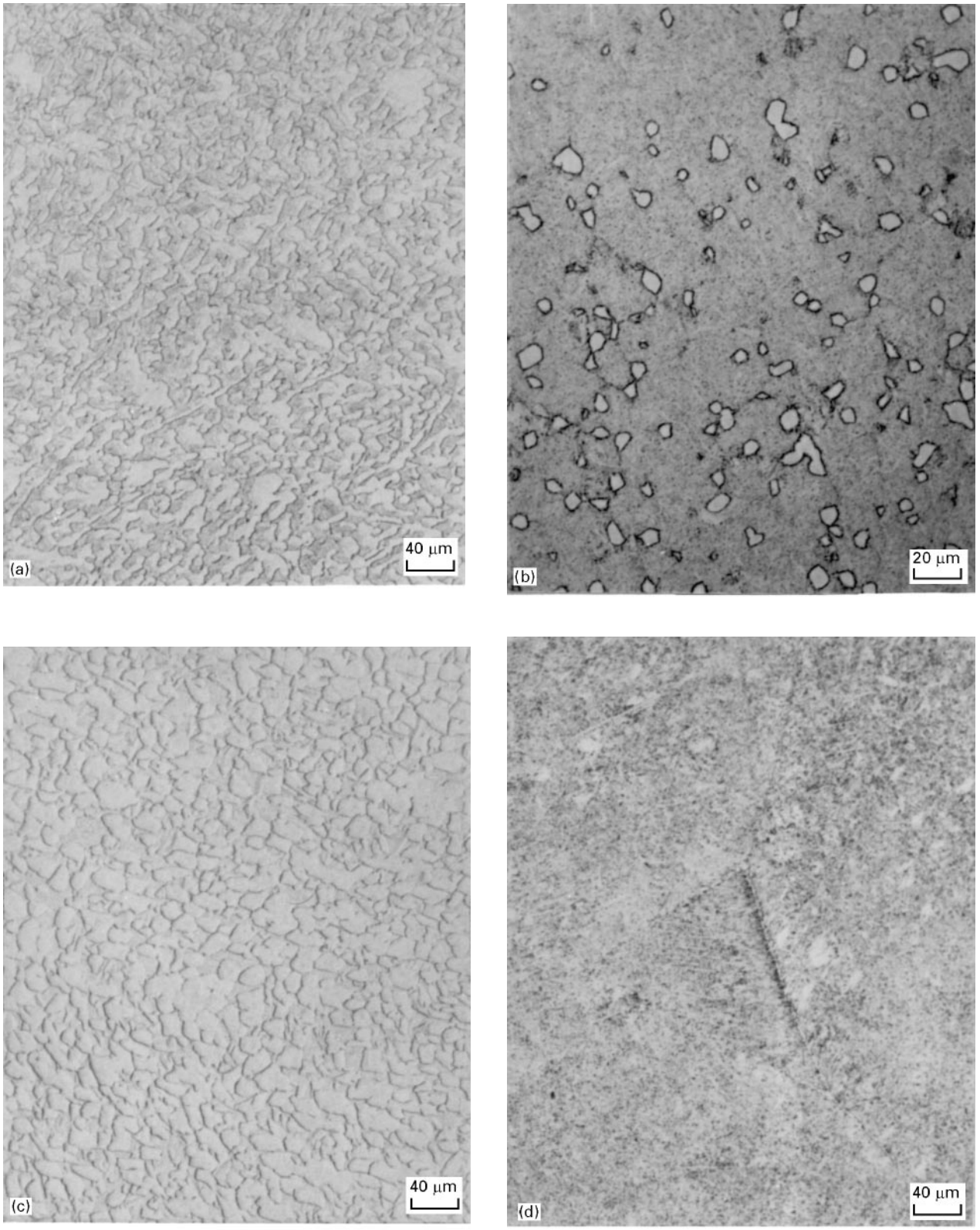

Figure 3 Effects of heat treatment on the microstructure of Ti–25Al–10Nb–3V–1Mo (a) 760 °C/24 h/AC, (b) 1045 °C/0.5 h/AC, (c) 1045 °C/0.5 h/FC + 760 °C/24 h/AC, and (d) 1200 °C/0.5 h/AC + 760 °C/45 h/AC.

due to mechanism changes that can occur with increasing initial strain rate. In general, the creep rates increased about half an order of magnitude between 540 and 650 °C, and a further half an order of magnitude between 650 and 760 °C (Fig. 7).

The creep exponents obtained are presented in Table II. The creep exponents obtained for material annealed in the β and $\alpha_2 + \beta$ phase fields were generally lower than those obtained for material annealed solely in the $\alpha_2 + \beta$ phase field, and the values obtained were between 3.2 and 7.7. These are comparable to previously reported data for α_2-based titanium aluminide [10, 11], and are in the range where creep deformation is expected to be dislocation-controlled [15]. The activation energies obtained for the different heat treatments at an initial stress level of 276 MPa

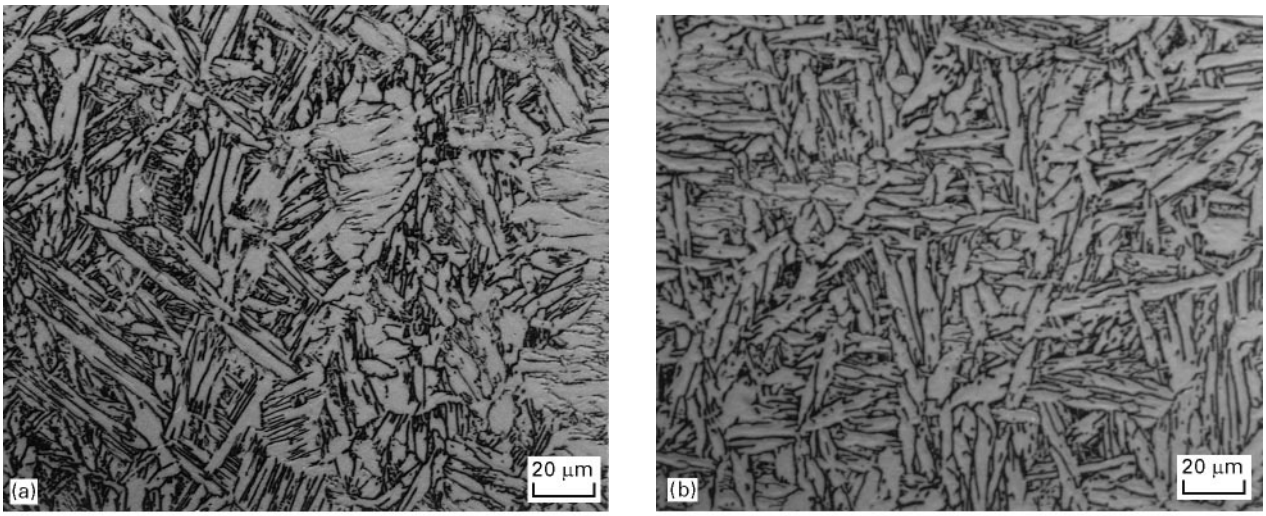

Figure 4 Effects of creep deformation at 760 °C for 20 h on the microstructure of Ti–24Al–11Nb (a) 815 °C/5.5 h/AC and (b) 982 °C/4 h/AC.

TABLE II Steady-state creep exponents obtained for Ti–24Al–11Nb

Temperature (°C)	Annealing schedule			
	1200 °C/0.5 h/AC + 760 °C/8 h/AC	1200 °C/0.5 h/AC + 815 °C/8 h/AC	815 °C/5.5 h/AC	982 °C/4 h/AC
540	4.1	3.6	6.2	6.3
650	3.2	4.3	7.7	6.2
760	3.3	5.8	6.1	5.1

TABLE III Activation energies obtained for Ti–24Al–11Nb at an initial stress level of 276 MPa

Annealing schedule	Activation energy (kJ mol^{-1})
1200 °C/0.5 h/AC + 760 °C/8 h/AC	211
1200 °C/0.5 h/AC + 815 °C/8 h/AC	243
815 °C/5.5 h/AC	303
982 °C/4 h/AC	208

are presented in Table III. The activation energies were between 208 and 303 kJ mol^{-1} in the microstructural conditions that were examined. The values obtained are also comparable to the activation energy of 305 kJ mol^{-1} reported by Cho *et al.* [11] for β-forged super-α_2 (Ti–25Al–10Nb–3V–1Mo) subjected to an initial stress level of 207 MPa.

The transmission electron microscopy study of deformation revealed some interesting substructural features/characteristics of deformation. These are summarized in Figs 8–10. There was evidence of a high degree of strain accommodation in the more ductile interdendritic β phase, as shown in Fig. 8. The deformation of material annealed at 1200 °C/0.5 h/AC + 815 °C/8 h/AC resulted in a moderate density of dislocation tangles of $b = \langle 1\,1\,2\,0 \rangle$ mixed dislocations in the α_2 phase (Fig. 9). The material annealed solely in the $\alpha_2 + \beta$ phase field at 982 °C/4 h/AC exhibited a variety of dislocation configurations and substructural features after creep deformation (Fig. 10). This included hexagonal networks of $b = \langle 1\,1\,2\,0 \rangle$ screw dislocations (Fig. 10a), dislocation tangles consisting of long, straight edge dislocations (Fig. 10b). Parallel arrays of straight $b = \langle 1\,1\,2\,0 \rangle$ screw dislocations were also observed in this material (Fig. 10c), and the orthorhombic phase [16] was present in some regions of the microstructure in which no dislocations or slip bands were observed (Fig. 10d). The presence of the orthorhombic phase, however, does not appear significantly to affect the secondary creep behaviour of the material annealed at 982 °C/4 h/AC, as shown in Fig. 6 and Tables II and III.

3.2. Ti–25Al–10Nb–3V–1Mo

The secondary creep rate data obtained for Ti–25Al–10Nb–3V–1Mo are presented in Fig. 11. Anomalous dual-slope secondary creep behaviour was observed at all temperatures, and the material with the so-called continuous microstructure (produced by annealing at 1045 °C/0.5 h/FC + 760 °C/24 h/AC) had better creep resistance than the material with the contiguous microstructure (produced by annealing at 760 °C/24 h/AC) at 650 and 760 °C. However, the contiguous microstructure generally resulted in lower creep rates at 540 °C. The lowest creep rates were obtained after two-stage annealing at 1200 °C/0.5 h/AC + 760 °C/45 h/AC. Unfortunately, however, this heat treatment resulted in a complete loss of the 4.6% room-temperature ductility of the as-received material. The effects of heat treatment on the room-temperature tensile properties of the Ti–24Al–11Nb and Ti–25Al–10Nb–3V–1Mo alloys are summarized in Table IV for comparison with the trends in the secondary creep rate data. In general, the ductility of the Ti–25Al–10Nb–3V–1Mo sheet was found to decrease with increasing secondary creep resistance, and no clear trend was established between the secondary creep data obtained and the tensile properties of the Ti–24Al–11Nb forging.

The creep exponents obtained for Ti–25Al–10Nb–3V–1Mo are presented in Table V. The creep

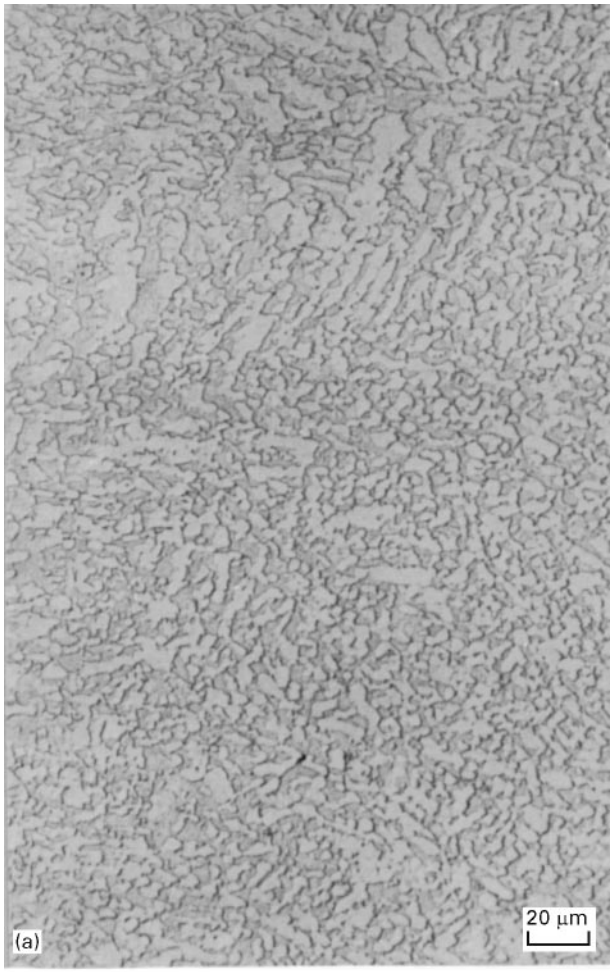

Figure 5 Effect of creep deformation at 760 °C for 20 h on the microstructure of Ti–25Al–10Nb–3V–1Mo (a) 760 °C/24 h/AC, (b) 1045 °C/0.5 h/FC + 760 °C/24 h/AC, and (c) 1200 °C/0.5 h/AC + 760 °C/45 h/AC.

exponents were somewhat higher than those obtained for Ti–24Al–11Nb (Table II), but comparable to those obtained in previous studies of the steady-state creep behaviour of β-forged Ti–25Al–10Nb–3V–1Mo [11]. They are also in the range where the micromechanisms

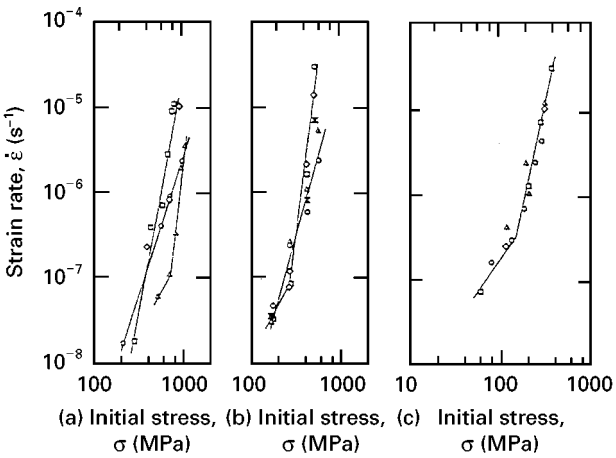

Figure 6 Effects of heat treatment on secondary creep rates in Ti–24Al–11Nb (a) 540 °C, (b) 650 °C, and (c) 760 °C.(○) HT_1, (△) HT_2, (□) HT_3, (◇) HT_4, (×) As-received. HT_1 = 1200 °C/0.5 h/AC − 815 °C/8 h/AC, HT_2 = 1200 °C/0.5 h/AC − 760 °C/8 h/AC, HT_3 = 815 °C/5.5 h/AC, HT_4 = 982 °C/4 h/AC.

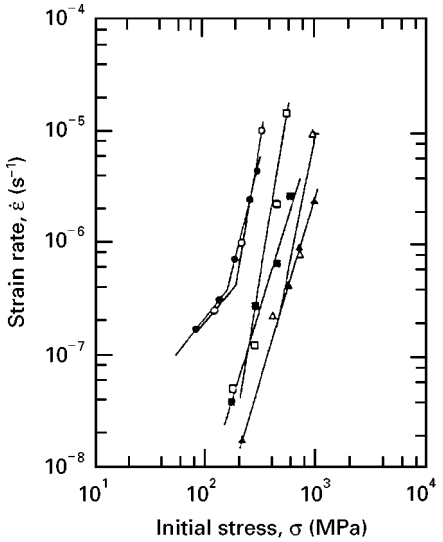

Figure 7 Effect of temperature on the secondary creep behaviour of Ti–24Al–11Nb. (▲ ■ ●) HT_1 = 1200 °C/0.5 h/AC + 760 °C/8 h/AC. (△, □, ○) HT_2 = 982 °C/4 h/AC. (▲, △) 540 °C, (■, □) 650 °C, (●, ○) 760 °C.

of creep deformation are expected to be dislocation-controlled [15]. The activation energies obtained for Ti–25Al–10Nb–3V–1Mo at a stress level of 276 MPa depended on which section of the dual-slope creep curves were employed. Extrapolation of the high strain-rate creep data resulted in much higher activation energies than those obtained from the analysis of the low strain-rate data (Table VI). As discussed previously for Ti–24Al–11Nb, similar anomalies have been observed for other α_2-based alloys [10, 11]. The reasons for these are not fully understood at present.

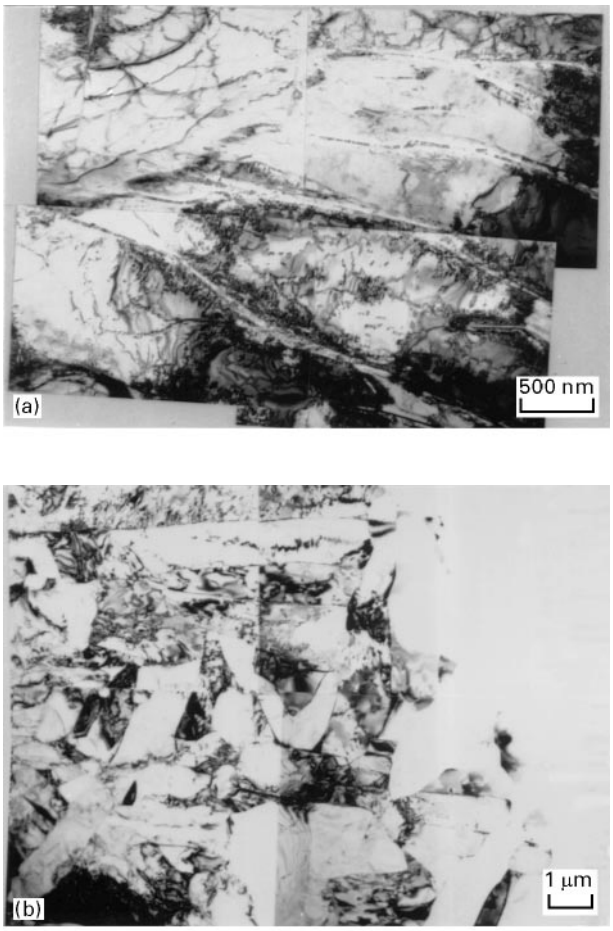

Figure 8 Bright-field transmission electron micrographs showing strain accommodation in the interdendritic β phase Ti–24Al–11Nb after creep deformation to 1.2% strain at 650 °C (initial stress = 345 MPa). (a) 1200 °C/0.5 h/AC + 815 °C/8 h/AC, and (b) 982 °C/4 h/AC.

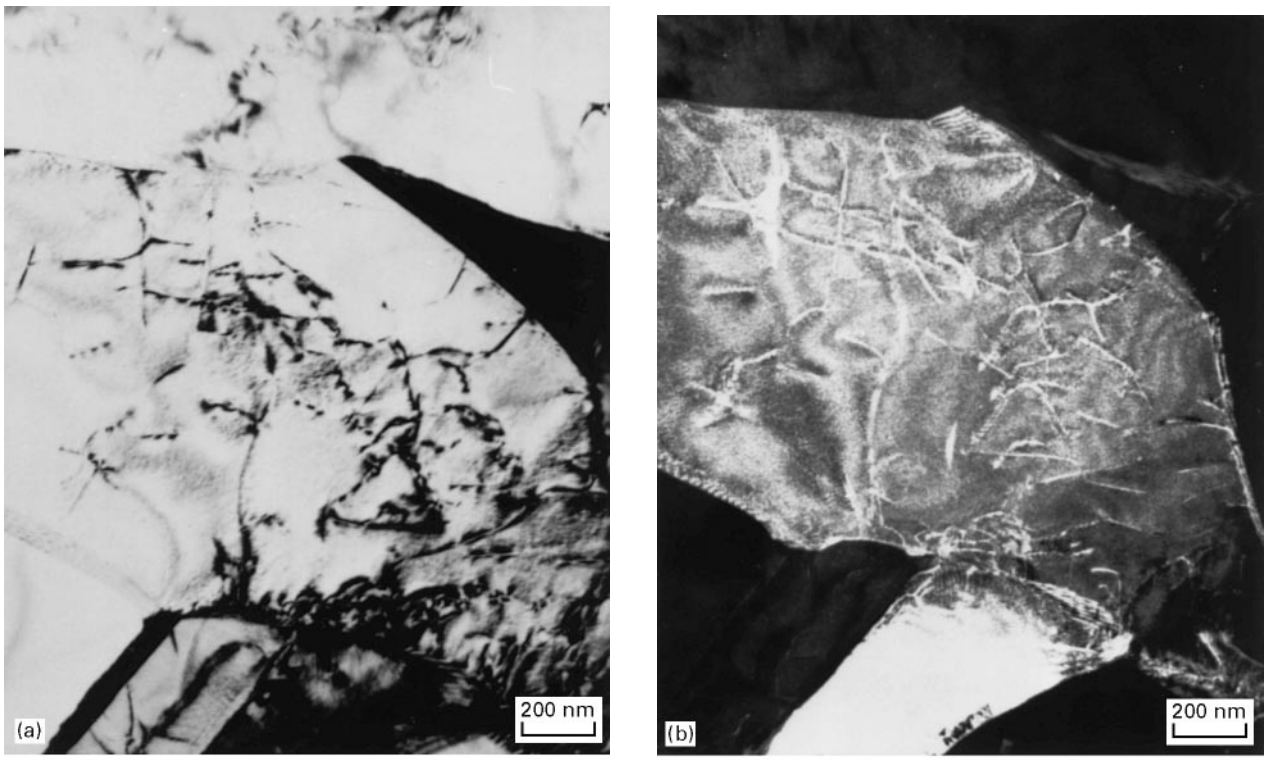

Figure 9 Dislocation substructures in Ti–24Al–11Nb annealed at 1200 °C/0.5 h/AC + 815 °C/8 h/AC and deformed under compressive creep conditions at 650 °C for 20 h (initial stress = 345 MPa); (a) bright-field image, and (b) weak-beam image.

4. Comparison of secondary creep data

The secondary creep rate data obtained for the $\alpha_2 + \beta$-forged Ti–24Al–11Nb and $\alpha_2 + \beta$-rolled Ti–25Al–10Nb–3V–1Mo are compared with previously reported data for β-forged Ti–25Al–10Nb–3V–1Mo [11] and two conventional β-processed near-α titanium alloys, i.e. Ti–6242S [12] and Ti–1100 [13], in Figs 12 and 13. The secondary creep rates obtained for Ti–24Al–11Nb and Ti–25Al–10Nb–3V–1Mo were generally lower than those obtained for Ti–6242S, and comparable to linear extrapolations of the Ti–1100 data. However, the lowest creep rates were observed in Ti–25Al–10Nb–3V–1Mo after annealing at 1200 °C/0.5 h/AC + 760 °C/45 h/AC (Fig.13). This resulted in creep rates that were comparable to those obtained by Cho *et al.* [11] for β-forged Ti–25Al–10Nb–3V–1Mo.

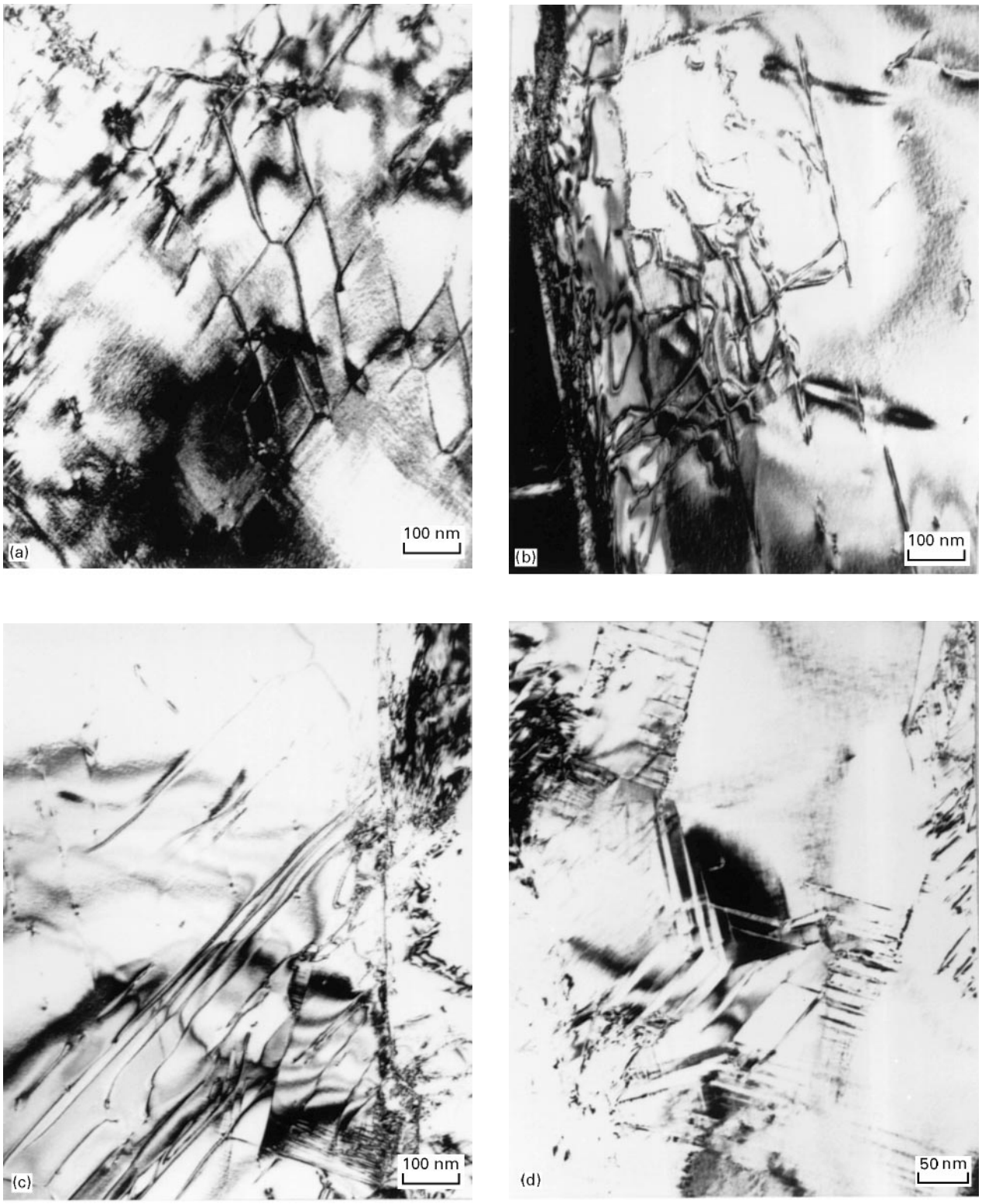

Figure 10 Substructures in Ti–24Al–11Nb annealed at 982 °C/4 h/AC and deformed under compressive creep conditions at 650 °C for 20 h (initial stress = 345 MPa). (a) Hexagonal networks of $b = \langle 1\,1\,\bar{2}\,0 \rangle$ screw dislocations, (b) dislocation tangles of $b = \langle 1\,1\,\bar{2}\,0 \rangle$ screw dislocations, $b = \langle 1\,1\,\bar{2}\,0 \rangle$ mixed dislocations, and $b = \langle 0\,0\,0\,1 \rangle$ edge dislocations, (c) parallel arrays of long straight $b = \langle 1\,1\,\bar{2}\,0 \rangle$ screw dislocations, and (d) orthohombic phase in "dislocation-free" regions.

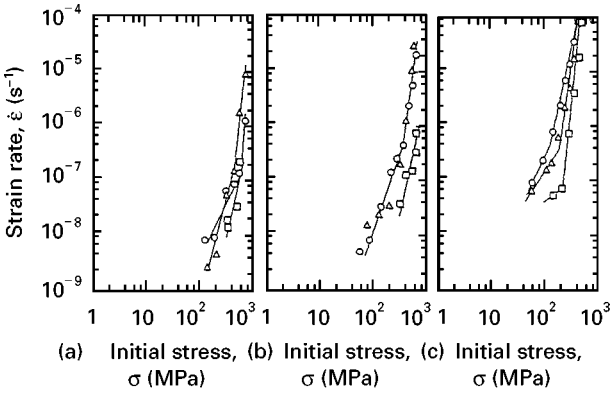

Figure 11 Secondary creep-rate data obtained for Ti–25Al–10Nb–3V–1Mo, (a) 540 °C, (b) 650 °C, and (c) 760 °C. (○) 760 °C/24 h/AC, (△) 1045 °C/0.5 h/AC + 760 °C/24 h/AC, (□) 1200 °C/0.5 h/AC + 760 °C/45 h/AC.

Finally. it is of interest to note that, with the exception of the data obtained for β-annealed Ti–25Al–10Nb–3V–1Mo, the secondary creep rates in the Ti–24Al–11Nb forging were similar to those obtained for the Ti–25Al–10Nb–3V–1Mo sheet (Fig. 14). This was rather surprising in view of the slower diffusion kinetics expected in Ti–25Al–10Nb–3V–1Mo [17]. However, it is important to note that the creep exponents that were obtained (Tables II and V) indicate dislocation-controlled, and not diffusion-controlled creep mechanisms. The propagation of slip/creep deformation will therefore be affected predominantly by the dislocation substructure and microstructural/substructural boundaries that resist the movement of dislocations through the lattice. The strain partitioning between the α_2 and β phases (Fig. 8) and the possible formation of third phases, may also play a role in the deformation process which is not fully understood at present.

5. Conclusions

For Ti–24Al–11Nb, the following conclusions were drawn.

1. Annealing in both the $\alpha_2 + \beta$ and β phase fields or solely in the $\alpha_2 + \beta$ phase field results in similar secondary creep rates in the Widmanstatten structures produced via forging and annealing close to the β solvus.
2. The activation energies for secondary creep deformation are between 208 and 303 kJ mol^{-1} for an initial stress level of 276 MPa and the microstructures that were examined.
3. The steady-state creep exponents are between 3.2 and 7.7 which suggests that secondary creep deformation is dislocation-controlled.
4. Strain partitioning occurs within the duplex $\alpha_2 + \beta$ microstructure during creep deformation which results in strain accommodation in the interdendritic β phase.

The following conclusions were drawn for Ti–25Al–10Nb–3V–1Mo

1. Annealing in the β phase field followed by air cooling and ageing in the $\alpha_2 + \beta$ phase field results in a Widmanstatten microstructure which was found to have the best creep resistance.
2. The so-called continuous $\alpha_2 + \beta$ microstructure (produced by annealing at 1045 °C/0.5 h/FC + 760 °C/8 h/AC) has better creep resistance than the contiguous $\alpha_2 + \beta$ microstructure (produced by

TABLE IV Effects of heat treatment on room-temperature tensile properties of Ti–24Al–11Nb and Ti–25Al–10Nb–3V–1Mo

Alloy	Heat treatment	0.2% offset yield stress (MPa)	Ultimate tensile stress (MPa)	Total strain to failure (%)	Plastic elongation to failure (%)
Ti–24Al–11Nb	As received (1093 °C/0.5 h/FAC)[a]	464	593	3.9	
	1200 °C/0.5 h/AC + 760 °C/8 h/AC	–[b]	582	–[b]	
	1200 °C/0.5 h/AC + 815 °C/8 h/AC	–[b]	502	–[b]	
	815 °C/5.5 h/AC	–[b]	340	–[b]	
	982 °C/4 h/AC	–[b]	356	–[b]	
Ti–25Al–10Nb–3V–1Mo	As received (982 °C/0.5 h/AC)[a]	862	986		4.6
	760 °C/24 h/AC	819	935		2.7
	1045 °C/0.5 h/AC + 760 °C/24 h/AC	1016	1063		0.5
	1200 °C/0.5 h/AC + 760 °C/45 h/AC	–[b]	740		–[b]

[a] As-received results included for comparison.
[b] Fractured before yield.

TABLE V Steady-state creep exponents obtained for Ti–25Al–10Nb–3V–1Mo

Temperature (°C)	Annealing schedule		
	760 °C/24 h/AC	1045 °C/0.5 h/FC + 760 °C/24 h/AC	1200 °C/0.5 h/AC + 760 °C/45 h/AC
540	7.7	7.3	7.5
650	7.0	8.0	5.8
760	4.3	6.2	7.2

TABLE VI Activation energies obtained for Ti–25Al–10Nb–3V–1Mo at an initial stress level of 276 MPa

Annealing schedule	Activation energy ($kJ\,mol^{-1}$)	
760 °C/24 h/AC	260	(338)[a]
1045 °C/0.5 h/FC + 760 °C/24 h/AC	223	(305)
1200 °C/0.5 h/AC + 760 °C/45 h/AC	243	(340)

[a] Parentheses indicate results obtained by extrapolating high strain-rate data.

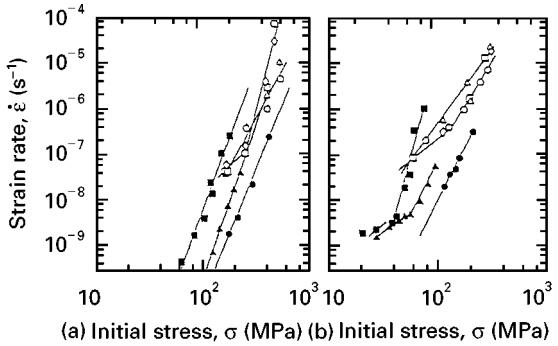

Figure 12 Comparison of the secondary creep behaviour in Ti–24Al–11Nb with data obtained for two near-α conventional titanium alloys ((■) Ti-6242S [12] and (▲) Ti-1100 [13]) and (●) β-forged Ti–25Al–10Nb–3V–1Mo [11]. (a) 650 °C and (b) 760 °C. (○) Ti–24Al–11Nb HT_1 = 1200 °C/0.5 h/AC + 760 °C/8 h/AC, (△) Ti–24Al–11Nb HT_2 = 1200 °C/0.5 h/AC + 815 °C/8 h/AC, (□) Ti–24Al–11Nb HT_3 = 815 °C/5.5 h/AC, (◇) Ti–24Al–11Nb HT_4 = 982 °C/4 h/AC.

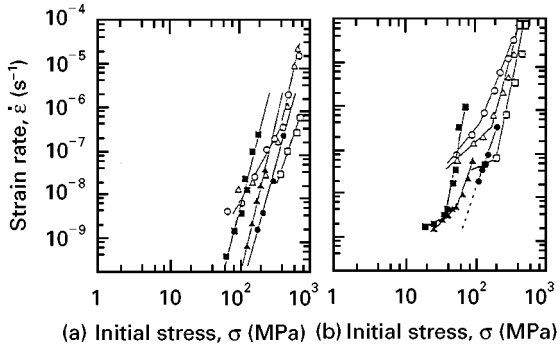

Figure 13 Comparison of the secondary creep behaviour in Ti–25Al–10Nb–3V–1Mo with data obtained for two near-α conventional Ti alloys ((■) Ti-6242S [12] and (▲) Ti-1100 [13]) and (●) β-forged Ti–25Al–10Nb–3V–1Mo. (a) 650 °C and (b) 760 °C. (○) 760 °C/24 h/AC, (□) 1200 °C/0.5 h/AC + 760 °C/45 h/AC, (△) 1045 °C/0.5 h/AC + 760 °C/24 h/AC.

annealing at 760 °C/4 h/AC) at 540 °C. However, the opposite is true at 650 and 760 °C.

3. The activation energies computed for secondary creep deformation are between 223 and 260 $kJ\,mol^{-1}$ when the anomalies in the slopes of the steady-state creep curves are included in the data analysis. Higher activation energies (305–338 $kJ\,mol^{-1}$) are computed using only high strain-rate data. Reasons for the dual-slope steady-state creep behaviour are unclear at present.

4. The steady-state creep exponents are between 4.3 and 8.0, which suggests that secondary creep deformation is dislocation-controlled.

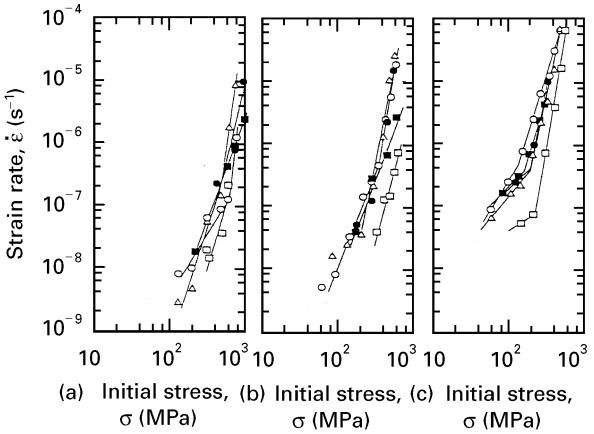

Figure 14 Comparison of the secondary creep behaviour of (■, ●) Ti–24Al–11Nb and (○, △, □) Ti–25Al–10Nb–3V–1Mo. (a) 540 °C, (b) 650 °C, and (c) 760 °C. (○) 760 °C/24 h/AC, (△) 1045 °C/0.5 h/FC + 760 °C/24 h/AC, (□) 1200 °C/0.5 h/AC + 760 °C/45 h/AC. (■) 1200 °C/0.5 h/AC + 760 °C/8 h/AC, (●) 982 °C/4 h/AC.

Comparison of secondary creep rates revealed the following points.

1. With the exception of β-processed/annealed (1200 °C/0.5 h/AC + 760 °C/45 h/AC) Ti–25Al–10Nb–3V–1Mo which resulted in the lowest steady-state creep rates, the steady-state creep rates were similar in Ti–24Al–11Nb and Ti–25Al–10Nb–3V–1Mo for all the microstructural conditions that were examined.

2. The secondary creep rates were generally lower than those reported for Ti–6242S, and comparable to linear extrapolations of values reported for Ti–1100 at higher strain rates.

3. The above comparisons are limited to structures similar to those discussed in this paper. Different trends may be observed in materials processed under different conditions that result in different microstructures.

Acknowledgements

The authors thank Dr Shankar M. L. Sastry, Dr Lee Semeatin and Dr Chuck Ward for useful discussions on the microstructural evolution and processing of α_2-based alloys. Appreciation is also extended to Messrs Jim D. Keyes, Jim J. Evans II, and Don J. Deuser for technical assistance. This research was initiated under the McDonnell Douglas Independent Research and Development Program. It was completed with the support of a Grant to W.O.S. from The Division of Materials Research of The National Science Foundation. The authors are grateful to the Program Monitor, Dr Bruce MacDonald, for his encouragement and support. Finally, the authors would like to thank Ms Liz Petersen and Ms Yingfang Ni for assistance in the preparation of the manuscript.

References

1. M. J. BLACKBURN and M. P. SMITH, "Improved Toughness Alloys Based on Titanium Aluminides", US Air Force Technical Report no. WRDC-TR-894095, Wright Patterson Air Force Base, Dayton, OH (1989).

2. B. J. MARQUARDT, G. K. SCARR, J. C. CHESNUTT, C. G. RHODES and H. L. FRASER, "Research and Development for Improved Toughness Aluminides", US Air Force Technical Report no. WRDC-TR-89-4133, Wright Patterson Air Force Base, Dayton, OH (1990).
3. Y. W. KIM, S. KRISHNAMURTHY, G. DAS and D. EYLON, "Microstructure Processing for Property Relationships and Interactions in Alloys", US Air Force Technical Report no. WRDC-TR-90-4021, Wright Patterson Air Force Base, Dayton, OH (1990).
4. M. J. BLACKBURN and J. C. WILLIAMS, *Trans. Am. Soc. Metals* **62** (1969) 398.
5. H. A. LIPSITT, D. SHECHTMAN and R. E. SCHAFRIK, *Metall. Trans.* **11A** (1980) 1369.
6. P. L. MARTIN, H. A. LIPSITT, N. T. NUHFER and J. C. WILLIAMS, in "Proceedings of the 4th International Conference on Titanium (Titanium 80)", edited by H. Kimuta and O. Izumi (TMS, Warrendale, 1990) pp. 1245–54.
7. C. H. WARD, J. C. WILLIAMS, A. W. THOMPSON, D. G. ROSENTHAL and F. H. FROES, *Mem. Etudes Sci. Rev. Metall.* October (1989) 647.
8. A. K. GOGIA, D. BANERJEE and T. .K. NANDY, *Metall. Trans.* **21A** (1990) 609.
9. D. L. DAVIDSON, K. S. CHAN and J. LANKFORD, "Crack Growth Processes at Elevated Temperatures in Advanced Materials," AFOSR Annual Technical Report for 1989, Southwest Research Institute Report no. SWRI-2699/7 (1990).
10. M. G. MENDIRATTA and H. A. LIPSITT, *J. Mater. Sci.* **15** (1980) 2985.
11. W. CHO, A. W. THOMPSON and J. C. WILLIAMS, *Metall. Trans.* **21A** (1990) 641.
12. M. J. BLACKBURN and M. P. SMITH, "R and D on Composition and Processing of Titanium Aluminide Alloys for Turbine Engines", US Air Force Technical Report no. AFWAL-TR-82-4086, Wright Patterson Air Force Base, Dayton, OH (1982).
13. W. CHO, J. W. JONES and J. E. ALLISON, unpublished research (1987).
14. A. W. THOMPSON, unpublished research, Carnegie Mellon University, PA (1991).
15. W. D. NIX and B. ILSCHNER, in "Strength of Metals and Alloys", Proceedings ICSMA5, edited by P. Haasen, V. Gerold and G. Kostorz (Pergammon Press, New York, 1980) pp. 1507–30.
16. D. BANERJEE, A. K. GOGIA, T. K. NANDI and V. A. HOSHI, *Acta Metall.* **36** (1988) 871.
17. C. H. WARD, *Int. Mater. Rev.* **38** (1993) 79.

Received 18 August 1995
and accepted 4 September 1996